Power generation from nanostructured PbTe-based thermoelectrics: Comprehensive development from materials to modules

Journal:	*Energy & Environmental Science*
Manuscript ID	EE-ART-09-2015-002979.R1
Article Type:	Paper
Date Submitted by the Author:	13-Nov-2015

Complete List of Authors:	Hu, Xiaokai; National Institute of Advanced Industrial Science and Technology (AIST), Jood, Priyanka; National Institute of Advanced Industrial Science and Technology (AIST), Ohta, Michihiro; National Institute of Advanced Industrial Science and Technology (AIST), Kunii, Masaru; National Institute of Advanced Industrial Science and Technology (AIST), Nagase, Kazuo; National Institute of Advanced Industrial Science and Technology, Nishiate, Hirotaka; National Institute of Advanced Industrial Science and Technology (AIST), Kanatzidis, Mercouri; Northwestern University, Department of Chemistry Yamamoto, Atsushi; National Institute of Advanced Industrial Science and Technology,

Power generation from nanostructured PbTe-based thermoelectrics: Comprehensive development from materials to modules†

Xiaokai Hu,[a] Priyanka Jood,[a] Michihiro Ohta,[a,*] Masaru Kunii,[a] Kazuo Nagase,[a] Hirotaka Nishiate,[a] Mercouri G. Kanatzidis,[b,c] Atsushi Yamamoto[a]

[a]*Research Institute for Energy Conservation, National Institute of Advanced Industrial Science and Technology (AIST), Tsukuba, Ibaraki 305-8568, Japan*

[*]*E-mail: ohta.michihiro@aist.go.jp*

[b]*Department of Chemistry, Northwestern University, Evanston, Illinois 60208, USA*

[c]*Materials Science Division, Argonne National Laboratory, Argonne, Illinois 60439, USA*

†Electronic Supplementary Information (ESI) available: Line scan of contact resistance between diffusion barrier and PbTe legs, thermal diffusivity and heat capacity, high-angle annular dark-field scanning transmission electron microscope image, calculated Lorenz number, multiple module testing data, thermoelectric properties of *p*- and *n*-type Bi_2Te_3, thermoelectric properties of diffusion barrier, and material's properties and geometrical parameters used for module simulation.

See DOI: 10.1039/x0xx00000x

Abstract

In this work, we demonstrate the use of high performance nanostructured PbTe-based materials in high conversion efficiency thermoelectric modules. We fabricated samples of PbTe–2% MgTe doped with 4% Na and PbTe doped with 0.2% PbI_2 with high thermoelectric figure of merit (ZT) and sintered them with Co–Fe diffusion barriers for use as *p*- and *n*-type thermoelectric legs, respectively. Transmission electron microscopy of the PbTe legs reveals two shapes of nanostructures, disk-like and spherical. The reduction in lattice thermal conductivity through nanostructuring gives a ZT of ~1.8 at 810 K for *p*-type PbTe and ~1.4 at 750 K for *n*-type PbTe. Nanostructured PbTe-based modules and segmented-leg modules using Bi_2Te_3 and nanostructured PbTe were fabricated and tested with hot-side temperatures up to 873 K in vacuum. The maximum conversion efficiency of ~8.8% for temperature difference (ΔT) of 570 K and ~11% for ΔT of 590 K have been demostrated in the nanostructured PbTe-based module and segmented Bi_2Te_3/nanostructured PbTe module, respectively. Three-dimensional finite-element simulations predict that the maximum conversion efficiency of the nanostructured PbTe-based module and segmented Bi_2Te_3/nanostructured PbTe module reaches to 12.2% for ΔT of 570 K and 15.6% for ΔT of 590 K respectively, which could be achived if the electrical and thermal contact between the nanostrucutred PbTe legs and Cu interconnecting electrodes is further improved.

1. Introduction

Greenhouse-gas emissions must be cut and energy management and sustainability must be improved in order to limit climate change to 2 degrees Celsius[1]. Because solid-state devices based on thermoelectrics can directly convert the waste heat generated from various sources such as industrial activity and automobiles into valuable electrical energy, thermoelectric waste heat recovery could make an important contribution to global sustainable energy solutions.[2–5]

A thermoelectric module, a key unit of the thermoelectric device, mainly consists of *p*- and *n*-type thermoelectric materials, which are connected electrically in series and thermally in parallel. The maximum efficiency of thermal to electrical energy conversion for a thermoelectric module is given by Carnot efficiency and average thermoelectric figure of merit $Z(T_\mathrm{h} + T_\mathrm{c})/2$ of the materials:[6]

$$\eta_{\max} = \frac{T_\mathrm{h}-T_\mathrm{c}}{T_\mathrm{h}} \frac{\sqrt{1+Z\frac{T_\mathrm{h}+T_\mathrm{c}}{2}}-1}{\sqrt{1+Z\frac{T_\mathrm{h}+T_\mathrm{c}}{2}}+\frac{T_\mathrm{c}}{T_\mathrm{h}}} \quad (1)$$

where T_h is the hot-side temperature and T_c is the cold-side temperature. Therefore, the performance of the module primarily depends on the *ZT* of the materials, defined as $ZT = (S^2T)/\rho\kappa_{\mathrm{total}}$, where *S* is the Seebeck coefficient, ρ is the electrical resistivity, κ_{total} is the total thermal conductivity, and *T* is the temperature. Extensive efforts have been devoted to development of high-*ZT* thermoelectric materials. Recently, the dramatic enhancements in *ZT* have been achieved by optimization of the power factor (S^2/ρ) and reduction in the thermal conductivity, as for example, PbTe[7–12], skutterudites[13–16], clathrates[17–19], half-heusler alloys[20–22], oxides[23–28], and sulfides[27–33].

Lead telluride, PbTe, has exceptional thermoelectric performance and has been used in thermoelectric generators such as radioisotope generator for the space missions

since 1960s[34]. Sodium and iodine are well known and effective acceptor and donor, respectively, for PbTe-based thermoelectric materials, as they yield controllable carrier concentration for enhanced S^2/ρ.[35,36]. The insertion of endotaxial nanostructures with proper band alignment in PbTe bulk materials has only a small effect on the electrical transport properties of the system, while it causes effective scattering of short-mean-free-path phonons, reducing the lattice thermal conductivity[37–46]. Moreover, the well-controlled mesoscale architecture of nanostructured materials leads to increase in scattering long-mean-free-path phonons at grain boundaries[47,48].

In 2004, the enhancement in *ZT* through nanostructuring bulk materials was first reported in $AgPb_mSbTe_{2+m}$[49]. Since then, a dramatic progress in the *ZT* has been made by nanostructuring and hierarchical architecturing. However, there has been little efforts to apply this progress in nanostructured materials to module development[50,51]. Along with *ZT,* the electrical and thermal contact resistances between thermoelectric materials and electrodes have considerable effects on the electrical power output and conversion efficiency of a module. To grow the thermoelectric market, increasing efforts should be devoted towards utilizing this progress in materials development into module development.

In this work, we have comprehensively developed nanostructured PbTe-based thermoelectrics and successfully demonstrated high *ZT* in the materials and, for the first time, corresponding high conversion efficiency in the modules. The sintered compacts of PbTe–MgTe doped with Na and PbTe doped with PbI_2 were used for *p*- and *n*-type legs of the modules, respectively. Transmission electron microscopy was used to characterize the ubiquitous MgTe nanoprecipitates in the *p*-type and the nanoscale intrinsic defects in both *p*- and *n*-type PbTe. The highest *ZT* achieved is ~1.8 at 810 K

for *p*-type PbTe–MgTe and ~1.4 at 750 K for *n*-type PbTe. Figure 1 shows the maximum conversion efficiency of the nanostructured PbTe–MgTe (*p*-type)–PbTe (*n*-type) module and segmented Bi_2Te_3 (*p*- and *n*-type)/nanostructured PbTe–MgTe (*p*-type)–PbTe (*n*-type) module developed in this study with important milestones achieved in previous studies[51–60]. The efficiency of ~8.8% obtained in the nanostructured PbTe (ns-PbTe)-based module for temperature difference (ΔT) of 570 K and ~11% obtained in the segmented Bi_2Te_3/ns-PbTe module for ΔT of 590 K are 40–50% higher compared to the previously reported efficiencies of non-nanostructured PbTe[52] module (~5.1% for ΔT of 417 K) and cascaded Bi_2Te_3/PbTe[55] module (~6.1% for ΔT of 485 K). As seen from Figure 1, our module efficiencies are among the highest achieved in the state-of-the-art thermoelectric modules. Three-dimensional finite-element simulations predict that the maximum conversion efficiency of the ns-PbTe-based module and segmented Bi_2Te_3/ns-PbTe module reaches to 12.2% for ΔT of 570 K and 15.6% for ΔT of 590 K respectively, which could be achieved if the electrical and thermal contact between the nanostrucutred PbTe legs and Cu interconnecting electrodes is further improved.

2. Experimental section

2.1. Materials preparation and characterization

2.1.1. Synthesis

Elemental lead (Pb; 99.9999%, Osaka Asahi Metal MFG), elemental tellurium (Te; 99.9999%, Osaka Asahi Metal MFG), elemental magnesium (Mg; 99.999%, Osaka Asahi Metal MFG), elemental sodium (Na; 99.95%, Sigma-Aldrich), and lead iodide

(PbI_2; 99.999%, Sigma-Aldrich) were used as starting materials without further purification. Amounts of 6.066 g of Pb, 3.891 g of Te, 0.015 g of Mg, and 0.028 g of Na were used to prepare *p*-type PbTe–2% MgTe doped with 4% Na. Amounts of 7.411 g of Pb, 4.555 g of Te, and 0.033 g of PbI_2 were used to prepare *n*-type PbTe doped with 0.2% PbI_2. A total of 10–12 g of the starting materials were well mixed under an N_2-filled glove box and loaded into a carbon-coated fused silica tube of 9 mm in outer diameter and 7 mm in inner diameter. The tubes were evacuated to a pressure of ~10^{-3} Pa and then flame-sealed. The mixtures were heated to 1323 K at a rate of ~70 K h^{-1}, held at 1323 K for 10 h, and then cooled to 873 K at a rate of ~11 K h^{-1}. The ingots were then cooled to room temperature over 15 h.

2.1.2. Sintering

The samples were sintered with and without diffusion barrier under a uniaxial pressure to fabricate the module and investigate the thermoelectric properties, respectively. In previous studies, Fe-, Nb-, and Ni-based alloys were used as the diffusion barriers[55,61–64]. In this study, we used Co–Fe alloy as a diffusion barrier to improve electrical and thermal contact between the thermoelectric legs and interconnecting electrodes. The electrical resistance at the interface of PbTe–2% MgTe doped with 4% Na and PbTe doped with 0.2% PbI_2 legs and Co–Fe diffusion barrier did not show any abrupt jump at room temperature, which confirms good electrical contacts (Figure S1 in Electronic Supplementary Information). An alloy of 80% Co (99.9%, Furuuchi Chemical)–20% Fe (99.998%, Furuuchi Chemical) was used as diffusion barrier for PbTe-based thermoelectric materials. The ingots of Na doped PbTe–2% MgTe and 0.2% PbI_2 doped PbTe were hand-ground to fine powders that were then

placed between the Co–Fe powders into graphite dies of 15 mm diameter. For each element, the graphite die was inserted into a sintering apparatus (SPS-515S, Fuji Electronic Industrial). The sintering was performed at 773 K for 1 h under a uniaxial pressure of 30 MPa in vacuum (7.0×10^{-3} Pa). The heating and cooling rates were 15 K min^{-1} and 20 K min^{-1}, respectively.

2.1.3. Powder X-ray diffraction and transmission electron microscopy

The phase purity of the synthetic powders and sintered compacts was examined by X-ray diffractometry (XRD; MiniFlex, Rigaku) using the Cu Kα radiations over the 2θ range of 10°–80°. The sintered compacts were crushed and hand-ground to measure the powder XRD patterns.

Transmission electron microscopy (TEM) and electron diffraction (ED) studies were performed using FEI Tecnai Osiris microscope operated at 200 kV. The TEM samples were prepared by polishing and Ar ion-milling.

2.1.4. Electrical transport measurements

The Seebeck coefficient and electrical resistivity were measured simultaneously under He atmosphere using a temperature differential method and four-probe method, respectively (ZEM-3, ULVAC-RIKO) over the temperature range of 300 K to 923 K. The typical dimensions of the bars used for the measurements were ~4 mm × ~3 mm × ~13 mm. The Seebeck coefficient and electrical resistivity were reproducible over the heating and cooling cycles for all samples. The relative uncertainty of the Seebeck coefficient and electrical resistivity is estimated to be within 5%.

The Hall coefficient (R_H) of the sintered compacts was measured at room

temperature with a home-built system under a magnetic field of 0 T to 2.3 T. The typical sample dimensions were ~5 mm × ~5 mm × ~0.3 mm. The Cu contact wires were attached to the samples using In-rich In-Ga paste.

2.1.5. Thermal transport measurements

The thermal conductivity (κ_{total}) was calculated from the thermal diffusivity (D), heat capacity (C_P), and sintered mass density (d) using the expression $\kappa_{total} = DC_Pd$. The thermal diffusivity was directly measured and the heat capacity was indirectly derived using a standard sample (Pyroceram 9606, Netzsch) using the laser flash method (LFA 457 MicroFlash, Netzsch) under the Ar gas flow atmosphere (100 ml min^{-1}) over the temperature range 300 K to 923 K. The samples for the measurements were typically square plates of ~10 mm × ~10 mm × ~2 mm. Graphite spray coating was applied on the sample surface. The thermal diffusivity was reproduced over heating and cooling cycles for all sintered compacts. The thermal diffusivity and heat capacity are provided in Figure S2 in Electronic Supplementary Information and the sintered mass density is provided in Table S1 in Electronic Supplementary Information.

The relative uncertainty of the thermal conductivity is estimated to be within 8%, taking into account the uncertainties for D, C_P, and d. The combined relative uncertainty for all measurements involved in the calculation of ZT is around 12%.

2.2. Module fabrication and characterization

2.2.1. Module fabrication

Thermoelectric legs of *p*- and *n*-type PbTe with $Co_{0.8}Fe_{0.2}$ diffusion barriers were prepared by grinding, polishing, and dicing of the sintered compacts (Figure 2(a)–(c)).

The cross section of legs is 2.0 mm × 2.0 mm. The lengths of the thermoelectric materials and diffusion barriers are 2.2 mm and 0.3 mm, respectively; the total length of legs is 2.8 mm.

The eight-couple (sixteen-leg) PbTe-based module was fabricated in the following procedures (Figures 2(d) and (e)). The *p*- and *n*-type legs were alternately positioned onto the insulated aluminum substrate with dimensions of 18 mm × 15 mm × 1 mm, where 105 μm thick Cu patterns were printed onto the 120 μm thick heat conducting polymer film (Yamagishi AIC). This substrate is well suited for thermoelectric module, because of its good thermal conductivity and electrical insulation. The legs were interconnected by the Cu electrodes of 5 mm × 2 mm × 1 mm. Liquid In–Ga eutectic alloy was smeared between legs and Cu interconnecting electrodes to reduce the electrical and thermal contact resistances. Two thick Cu leading wires and two thin Cu wires were soldered to the Cu pattern to supply the electrical current and measure the terminal voltage, respectively.

A similar procedure was applied for the fabrication of segmented module (Figures 2(f) and (g)). Commercial *p*- and *n*-type bismuth telluride (Sb_2Te_3–Bi_2Te_3-based alloy; Ferrotec Nord) were used as the low-temperature legs. The Bi_2Te_3 legs of 2.0 mm× 2.0 mm × 2.0 mm and nanostructured PbTe legs of 2.0 mm× 2.0 mm × 2.8 mm (the total length of segmented legs: 4.8 mm.) were connected by In–Ga liquid metal. Each leg had diffusion barrier layers, electro-plated nickel for Bi_2Te_3 and co-sintered $Co_{0.8}Fe_{0.2}$ for PbTe, to prevent the In–Ga diffusion into the materials at elevated temperature.

2.2.2. Module testing

The electrical power output and conversion efficiency of nanostructured PbTe–

MgTe (*p*-type)–PbTe (*n*-type) and segmented Bi_2Te_3 (*p*- and *n*-type)/nanostructured PbTe–MgTe (*p*-type)–PbTe (*n*-type) modules were measured using a hot-side temperature of 873 K, 773 K, 673 K and 573 K in vacuum (1.0 Pa) in a home-built testing system[65]. The cold-side temperature was maintained at 283 K or 303 K. Figure 3 shows a photograph of the module testing system. The modules were mounted between AlN ceramic plates. The heater, AlN ceramic plates, module, and Cu blocks were pressed by a pneumatic cylinder under a uniaxial pressure of 0.22 kN to reduce the electrical and thermal contact resistances. Peltier cooling devices were placed on the bottom of Cu base to maintain the cold-side temperature at 283 K or 303 K. Graphite sheet (110 μm thick, Grafoil) and thermal grease (KS-613, Shin-Etsu Silicone) were used to reduce further the thermal contact resistances between the Cu blocks and AlN ceramic plates and between the AlN ceramic plates and module. The hot- and cold-side temperatures of the module, T_h and T_c, were measured by using thermocouples embedded in the AlN ceramic plates.

An oxygen-free Cu block with known thermal conductivity (κ_{Cu}) having a size of 15 mm × 15 mm × 60 mm was used as a heat flow meter. Six thin Pt resistance thermometers (Pt100, 1 mm diameter) were embedded in the Cu block at a vertical distance (L_{Pt100}) of 40 mm to each other in order to measure the temperature drop ΔT along the heat flow direction. The T_h and T_c of the Cu block were measured by their respective three Pt resistance thermometers. The heat dissipated from the cold side of the module (Q_c) was calculated in accordance with one-dimensional Fourier's law; $Q_c = \kappa_{Cu}\Delta T(A_{Cu}/L_{Pt100})$, where A_{Cu} is cross-sectional area of Cu block.

A direct current electronic load (PLZ164WA, Kikusui Electronics) was connected to the module for supplying the electrical current to measure the electrical power output

P. The conversion efficiency η was calculated using Equation (2).

$$\eta = \frac{P}{P+Q_c} \quad (2)$$

The uncertainty of heat flow is estimated to be within ±3%; therefore the uncertainty for efficiency measurement is estimated to be the same (within ±3%).

2.2.3. Module simulation

The electrical power output and conversion efficiency of our nanostructured PbTe–based module and segmented Bi_2Te_3/nanostructured PbTe module were investigated by three-dimensional finite-element simulation in COMSOL Multiphysics[66–70]. The thermoelectric effect in a steady state can be expressed by a set of differential equations (3–6) with temperature (*T*) and electric potential (*V*) as two unknowns[66,69–71]. Electrical current density (*J*) and heat flux (*q*), as intermediate variables, are vectors in three spatial directions with a unit of A/m^2 and W/m^2, respectively.

$$J = \sigma(-\nabla V - S\nabla T) \quad (3)$$

$$q = -k_{\text{total}}\nabla T \quad (4)$$

$$\nabla J = 0 \quad (5)$$

$$\nabla(k_{\text{total}}\nabla T) + J^2/\sigma - TJ\nabla S = 0 \quad (6)$$

where σ denotes the electrical conductivity, equivalent to inversed resistivity.

The three-dimensional distribution of *J*, *q*, *V,* and *T* were numerically solved under given electrical and thermal boundary conditions. Important values which characterize the module such as electrical current *I*, terminal voltage *V*(*I*), heat dissipated from the cold side of the module $Q_c(I)$, electrical power output *P*(*I*), were calculated from *J*, *q*, *V* and *T.* More precisely, $Q_c(I)$ was estimated by using either area integration of *q* over the bottom substrate of the module, and *P* was determined by volumetric integration of

Joule heat J^2/σ inside the electrical load resistance in the model. Experimental control parameters such as hot- and cold-side temperatures T_h and T_c and electrical load resistance R_L were changed by a parametric sweep function of the software to simulate the real module testing. The efficiency η of the module was then determined using Equation 2 as a function of current I. Total time required for the simulation of current–voltage curves at certain temperature difference was several tens of seconds using a high-end personal computer.

A geometrical model was created in the software interface to represent nanostructured PbTe-based module with an identical dimension. The model was composed of an aluminum substrate with insulated polymer film and Cu patterns, *p*- and *n*-type nanostructured PbTe, $Co_{0.8}Fe_{0.2}$ diffusion barriers, and Cu interconnecting electrodes. The model also contained an electrical load resistance connected to two output terminal electrodes of the module. The load resistance was assumed to be thermally connected with an infinite heat sink so that there is neither temperature rise of the load nor backflow of heat to the module during the power generation. It should be noted that electrical and thermal contact resistance and radiation effects are not taken into account in the simulation model. The electrical and thermal transport coefficients (S, ρ, and k_{total}) of *p*- and *n*- PbTe and $Co_{0.8}Fe_{0.2}$ taken from the measured data are expressed as third order polynomials, while those for the Cu interconnecting electrodes and insulated aluminum substrate were assumed to be constant.

3. Results and discussion

3.1 Crystal structure and nanoscale structures

Powder X-ray diffraction (XRD) patterns of PbTe–2% MgTe doped with 4% Na

(*p*-type) and PbTe doped with 0.2% PbI_2 (*n*-type) are consistent with the face-centered-cubic PbTe structure with $Fm\bar{3}m$ space group (Figure 4). No secondary phases are observable within the detection limits of the measurement.

The nanostructures of both the systems were investigated by means of transmission electron microscopy (TEM). Figures 5(a) and (b) show typical mid-magnification TEM bright field images of *p*-type PbTe–MgTe and *n*-type PbTe, respectively. The images reveal nanostructures as dark contrasts embedded in the PbTe matrix. Electron diffraction patterns along [001] zone axis (inset of Figures 5(a) and (b)) including both matrix and nanostructures exhibit no split spots which confirms that these nanostructures are endotaxially embedded in the matrix.

Figures 5(c) and (d) show high-magnification TEM images of *p*-type PbTe–MgTe and *n*-type PbTe, respectively. While two shapes of nanostructures, disk-like and spherical, were observed in *p*-type leg, only disk-like nanostructures were observed in *n*-type leg. The typical diameter of spherical nanoprecipitates found only in the *p*-type leg is 3 nm–5 nm. The TEM experiment reveals the coherent nature of interface between the spherical nanoprecipitates and the matrix which is necessary to maintain high power factor[41,42,44], as we will see below. The dark regions representing the lattice strain fields can be seen surrounding the precipitates which provide phonon scattering and reduce the lattice thermal conductivity.

The disk-like nanostructures which are observed for both *p*-type PbTe–MgTe and *n*-type PbTe legs are about 2–5 nm in length and possibly 1–2 atomic layers thick. Bright lobe-like regions seen on each side of these nanostructures represent the lattice strain fields. Their presence in both *p* and *n*-type legs suggests that they are not induced by MgTe and do not comprise of dopant atoms (Na and I). These intrinsic disk-like

nanostructures have been observed by many authors and were interpreted differently in each case, such as Te vacancies[72], Pb vacancies[73], or nanoprecipitates[46–48]. It is difficult to characterize them through energy dispersive X-ray spectrometry due to their small size. In our previous study on *n*-type $PbTe_{1-x}I_x$, we confirmed the presence of Pb precipitates (~5 μm) in the sample[74].

Figure 5(e) is the high-angle annular dark-field scanning transmission electron microscope image of *p*-type leg which shows the presence of microscale spherical precipitates with an average diameter of ~150 nm. Energy dispersive spectroscopy analysis (Figure 5(f)) carried out on the microcrystals confirms the composition close to MgTe as they appear Mg rich but Pb and Na deficient. No such microscale precipitates were observed in the *n*-type leg (Figure S3 in Electronic Supplementary Information).

3.2 Thermoelectric properties

Carrier concentration (n) measured through room temperature Hall effect measurements and the Hall mobility (μ) derived from the equation $\mu = 1/\rho ne$ (e: electronic charge), for both the materials are presented in Table 1. The μ and n of our PbTe samples are consistent with the earlier reported work on this system[36,48]. For example, the n and μ of our *p*-type PbTe–MgTe is ~9.5×10^{19} cm^{-3} and ~130 $cm^2\ V^{-1}\ s^{-1}$, respectively, which is similar to the values reported previously for the similar composition sintered PbTe ($n \sim 1.02\times10^{20}$ cm^{-3}; $\mu \sim 90$ $cm^2\ V^{-1}\ s^{-1}$)[48]. The sign of both, the Hall coefficient (R_H) (Table 1) and Seebeck coefficient (S) (Figure 6(a)), is positive for *p*-type PbTe–MgTe and negative for *n*-type PbTe indicating carrier transport by holes and electrons, respectively.

Figures 6(a) and (b) show the temperature dependence of the Seebeck coefficient

(S) and electrical resistivity (ρ) of p-type PbTe–2% MgTe doped with 4% Na and n-type PbTe doped with 0.2% PbI_2, respectively. The data are consistent with the degenerate semiconducting behaviour, where, ρ and S increase with temperature. The room temperature ρ for both the samples is ~5 μΩ m (~0.5 mΩ cm), which increases to ~27 μΩ m (~2.7 mΩ cm) and ~34 μΩ m (~3.4 mΩ cm) at 900 K for p- and n-type samples, respectively. While n-type ρ increases at a fast rate at high temperature (above 600 K), the p-type ρ becomes relatively steady. The S (Figure 6(a)) of p-type PbTe increases linearly with temperature untill ~600 K, above which its rate of increase become considerably smaller.

The slow rate of increase in ρ and S for p-type PbTe can be explained using the two valence band model[35]. At room temperature, the light hole valence band mainly contributes to the electrical properties, while at high temperatures, both valence bands (light and heavy) contribute to charge transport as holes are excited thermally to the heavy hole valence band. This leads to a dynamic increase in n resulting in a slower increase of ρ with temperature. Due to a nearly steady ρ and S for a wide temperature range of 500 to 900 K, a broad temperature plateau in the power factor (S^2/ρ) (Figure 6(c)) was obtained for p-type PbTe–MgTe, which is important in achieving the high electrical power output and conversion efficiency of our module.

The coherent disk-like and spherical nanostructures retain the μ, maintaining the high S^2/ρ in PbTe system. For example, our p-type power factor (~2200 μW K^{-2} m^{-1} (~22 μW K^{-2} cm^{-1}) at 900 K) is similar to the nanostructured PbTe-2% MgTe doped 2% Na_2Te ingot sample (~2500 μW K^{-2} m^{-1} (~25 μW K^{-2} cm^{-1}) at 800 K)[44] and nanostructured PbTe-2% MgTe doped 2% Na sintered sample (~2500 μW K^{-2} m^{-1} (~25 μW K^{-2} cm^{-1}) at 900 K)[48]. The power factor of our n-type samples peak at ~600 K with

a value of ~2200 μW K^{-2} m^{-1} and lowers slightly at high temperatures (~1500 μW K^{-2} m^{-1} (~15 μW K^{-2} cm^{-1}) at 900 K). These power factor values are among the highest reported for *n*-type PbTe system[36,75,76].

Figure 6(d) shows the temperature dependence of the total thermal conducitvity (κ_{total}) and lattice thermal conductivity (κ_{lat}) of *p*-type PbTe–2% MgTe doped with 4% Na and *n*-type PbTe doped with 0.2% PbI_2. The κ_{total} of both the systems is ~1.2 W K^{-1} m^{-1} at 900 K. The κ_{lat} was determined by substracting the electronic thermal conductivity (κ_{el}) given as $\kappa_{el} = LT/\rho$ (L is the Lorenz number) from the κ_{total}. The L can be expressed as a function of the reduced chemical potential (ζ^*) for a single parabolic band[77,78]:

$$L = \left(\frac{k_b}{e}\right)^2 \frac{3F_0(\zeta^*)F_2(\zeta^*) - 4F_1(\zeta^*)^2}{F_0(\zeta^*)^2} \quad (7)$$

ζ^* was obtained from the fitting of the experimental S values using the following equation for the single parabolic band model dominated by acoustic phonon scattering:

$$S = \frac{k_b}{e}\left(\frac{2F_1(\zeta^*)}{F_0(\zeta^*)} - \zeta^*\right) \quad (8)$$

The Fermi integrals $F_m(\zeta^*)$ are defined as:

$$F_m(\zeta^*) = \int_0^\infty \frac{x^m}{1+\exp(x-\zeta^*)} dx \quad (9)$$

where x is the reduced energy of carriers. The temperature dependence of the calculated L from the fitting procedure for *p*- and *n*-type PbTe is given in Figure S4 in Electronic Supplementary Information. For example, the L of both the systems is estimated as ~2.1 $\times 10^{-8}$ W Ω K^{-2} and ~1.6 $\times 10^{-8}$ W Ω K^{-2} at 300 K and 900 K, respectively. The room temperature κ_{lat} of the *p*- and *n* type samples is ~2.1 W K^{-1} m^{-1} and ~2.4 W K^{-1} m^{-1}, respectively which decreases to ~0.7 W K^{-1} m^{-1} and ~ 0.8 W K^{-1} m^{-1} at 900 K. Such low κ_{lat} is a result of enhanced phonon scattering from spherical nanoprecipitates (in

p-type) and disk-like nanoprecipitates (in *p*- and *n*-type) in our samples.

The thermoelectric figure of merit (*ZT*) of *p*-type PbTe–2% MgTe doped with 4% Na and *n*-type PbTe doped with 0.2% PbI_2 are shown in Figure 7. Low κ_{lat} owing to nanostructuring and high S^2/ρ for a wide temperature range result in a high *ZT* for *p*-type with a maximum value of ~1.8 at 800 K. A slightly lower maximum *ZT* (~1.4) at 750 K was achieved for *n*-type PbTe. These *ZT* values are among the highest achieved for both, *p*- and *n*-type PbTe systems.

3.3 Conversion efficiency of the nanostructured module

The terminal voltage (*V*), electrical power output (*P*), heat dissipated from the cold side of the module (Q_c), and conversion efficiency (η) of the nanostructured PbTe–2% MgTe doped with 4% Na (*p*-type)–PbTe doped with 0.2% PbI_2 (*n*-type) module (ns-PbTe-based module) comprising eight *p*–*n* couples are shown as functions of electric current *I* in Figure 8. The slope of the *V*-*I* curve (Figure 8(a)) approximately gives the internal resistance of the module. The resistance increases from ~100 mΩ for temperature difference (ΔT) of 270 K to ~150 mΩ for ΔT of 570 K, because the electrical resistivity of *p*- and *n*-type legs increases with temperature ((Figure 6(b)). The *y*-intercept on *V*-*I* curve is the open-circuit voltage (V_{OC}), which nearly corresponds to the Seebeck voltage of the 16 legs. The V_{OC} increases from ~0.57 V for ΔT of 270 K to ~1.47 V for ΔT of 570 K, because the Seebeck coefficient of *p*- and *n*-type ns-PbTe increases with temperature (Figure 6(a)).

The *P* (Figure 8(b)) is calculated from *V* and *I*, $P = VI$. The value of *P* reaches a maximum when the impedance is matched between the external electronic load and the internal resistance (R_{in}) of the ns-PbTe-based module. For example, the *P* for ΔT of 570

K increases with increasing I, reaching a value of ~3.3 W at 3.5 A. The maximum power output (P_{max}) increases from ~0.84 W (~0.37 W cm^{-2}) for ΔT of 270 K to ~3.6 W (~1.6 W cm^{-2}) for ΔT of 570 K.

As shown in Figure 8(c), the Q_c increases with the current, because of the Peltier heating and Joule heating, which are proportional to the current and to square of the current, respectively[79]. The open-circuit heat flow (Q_{oc}), the y-intercept on the plot, involve heat conduction through the legs and possible heat leakage by radiation, which causes underestimation of the conversion efficiency.

The η also reaches a maximum when the impedance between the external load and the internal resistance of the module matches. For example, the η for ΔT of 570 K increases with increasing current, reaching a maximum value (η_{max}) of ~8.8% at 4.3 A. This high η_{max} results from the high performance of the nanostructured PbTe–MgTe doped Na (p-type) and PbTe doped PbI_2 (n-type) materials, and is more than 40% higher than the efficiency of non-nanostructured PbTe module[52].

The module testing was performed four times on the same module to confirm the reproducibility. The P and η showed a weak hysteresis during the first measurement. In the subsequent second, third, and fourth measurements, we observed good repeatability reproducing the data within 2%, keeping the high performance as shown in Figure S5 in Electronic Supplementary Information. In addition, the nanostructured PbTe-based module withstood the mechanical load of 0.22 kN under large temperature gradients, such as 570 K and no crack and deformation were observed even after testing four times. This result implies not only the stable nature of nanostructured PbTe at elevated temperature in vacuum for short duration testing (several hours), but also the

effectiveness of our module fabrication technique. Our future work will involve a study on the long-life stability of these modules.

3.4 Simulation of the nanostructured module

Power generation characteristics of our ns-PbTe-based module were investigated in COMSOL Multiphysics with measured thermoelectric properties of legs. The materials' properties for the simulation are shown in Table S2 in Electronic Supplementary Information.

The results of the numerical simulations are shown in Figure 9. The input geometry is the same as that of the ns-PbTe-based module fabricated in this work (Figure 9(a)). The geometrical parameters are shown in Table S2 in Electronic Supplementary Information. The distributions of temperature (T) and electrical potential (V) are shown in Figure 9(b) and Figure 9(c), respectively. The temperature gradient occurs across the length of the PbTe legs (Figure 9(b)). The V increases from the cathode to the anode inside the module (Figure 9(c)). The z-component of the heat flow visualized in Figure 9(d) are integrated over the surface of Cu interconnecting electrodes and the surface of the bottom insulated aluminum substrate to provide the total amount of heat absorbed at the hot side of the module (Q_h) and the heat dissipated from the module at the cold side (Q_c). Figure 9(e) shows the distribution of joule heat in the module and in the electrical load resistance. The red color in the load resistance shows that the power generated from the module is consumed as joule heat. A volumetric integration of the joule heat density in the load resistance gives the electrical output power (P) of the module, which is also derived from $P = IV$. Figure 9(f) shows the distribution of the ZT of the used

thermoelectric materials and diffusion barriers under large temperature gradient of 570 K, which is a good reproduction of the measured *ZT* shown in Figure 7.

The simulated V, P, Q_c, and η as functions of I are shown in Figure 10. The simulated V_{oc}, R_{in}, P_{max}, Q_{oc} and η_{max} are summarized in Table 2 along with the measured values. For ΔT of 570 K, the measured P_{max} and η_{max} are ~3.6 W and ~8.8%, which are ~25% lower than the simulated values (P_{max} = 4.71 W and η_{max} = 12.2%). The reason for the lower values of measured P_{max} and η_{max} is the lager internal electrical resistance (R_{in}) of the fabricated module. As shown in Table 2, the measured R_{in} for ΔT of 570 K is ~0.15 Ω and this is 10% larger than the ideal value of 0.137 Ω. The difference in R_{in} between measurement and simulation is caused by the imperfect jointing at the materials interfaces. There is a possibility of the deterioration of Co-Fe diffusion barrier at elevated temperatures, which could also increase R_{in}. Further optimization of the jointing and the relevant materials interfaces presumably will enable higher P and η.

The larger value of measured Q_c also leads to lower value of measured η_{max}. The measured Q_{oc} of ~31 W at ΔT of 570 K is ~13% larger than simulated values of 27.3 W. The deviation of ~3.7 W can be explained by the radiation heat exchange in the module. The net radiative heat is described as:[80]

$$Q_{rad} = 5.67 \times 10^{-8} \cdot \varepsilon \cdot A(T^4{}_h - T^4{}_c) \qquad (10)$$

where Q_{rad}, ε, and A are the radiative heat flow, emissivity of the material and exposed area, respectively. In the fabricated module, the sixteen-legs occupy only 24% of the area of the module substrate. The rest of the open area provides a radiation transfer path. If the emissivity of the substrate is 0.5, the parasitic radiation heat flow is calculated to be 3.2 W for the hot-side temperature T_h = 873 K and cold-side temperature T_c = 303 K.

This value accounts well for the deviation between the simulation and measurement and strongly indicates that the heat conduction observed in the PbTe legs is almost equal to the ideal values calculated based on the thermal conductivity data.

3.5 Conversion efficiency and simulation of the segmented module

With segmentation η_{max} generally improves because of the rise in the leg average *ZT* over the entire temperature range, as shown in Equation (1). The segmented *p*- and *n*-type Bi_2Te_3/nanostructured PbTe (Bi_2Te_3/ns-PbTe) legs have been fabricated to boost the average *ZT*. The ns-PbTe-based legs have high *ZT* in the high temperature range of 500 K to 900 K, while the Bi_2Te_3-based legs have high *ZT* in the low temperature range of 280 K to 400 K (Figure S6 in Electronic Supplementary Information). Therefore, in the segmented Bi_2Te_3/ns-PbTe leg, both the materials complement each other by helping to cover a much wider temperature range of high *ZT*.

Figure 11 shows the measured V, P, Q_c, and η of segmented Bi_2Te_3/ns-PbTe (Bi_2Te_3/PbTe–MgTe (*p*-type)–Bi_2Te_3/PbTe (*n*-type)) module as functions of I. The V_{oc}, R_{in}, P_{max}, Q_{oc}, and η_{max} are summarized in Table 3. It is interesting to compare the values observed in the segmented Bi_2Te_3/ns-PbTe module with those observed in the ns-PbTe module. The V_{OC} of the segmented Bi_2Te_3/ns-PbTe module (Figure 11(a)) is larger than that of the ns-PbTe module (Figure 8(a)), because of the larger average Seebeck coefficient of segmented Bi_2Te_3/ns-PbTe leg. For example at T_h = 873 K the V_{OC} is ~1.86 V for the segmented Bi_2Te_3/ns-PbTe module and ~1.47 V for the ns-PbTe module. The larger R_{in} in the segmented Bi_2Te_3/ns-PbTe module is due to the higher length of segmented legs and electrical contact resistances between PbTe and Bi_2Te_3. The R_{in} of the segmented Bi_2Te_3/ns-PbTe module is more than two times that for the

ns-PbTe module; at T_h = 873 K, the R_{in} of the segmented Bi_2Te_3/ns-PbTe and ns-PbTe modules are ~370 mΩ (Table 3) and ~150 mΩ (Table 2), respectively.

The V_{OC} for the segmented Bi_2Te_3/ns-PbTe module is larger than that for ns-PbTe module, however, due to the larger R_{in}, the corresponding P of the segmented Bi_2Te_3/ns-PbTe module is lower than that of ns-PbTe module (Figure 11(b) and Figure 8(b)). At T_h = 873 K, the P_{max} is ~2.34 W for segmented Bi_2Te_3/ns-PbTe module (Table 3) and ~3.55 W for ns-PbTe module (Table 2).

Since the thermal contact resistance of the segmented Bi_2Te_3/ns-PbTe module is larger than that of ns-PbTe module, the Q_c is nearly one half that of the latter (Figure 11(c) and Figure 8(c)). For example at T_h = 873 K, the Q_{oc} of the segmented Bi_2Te_3/ns-PbTe and ns-PbTe modules is ~16 W (Table 3) and ~31 W (Table 2), respectively.

The measured η as a function of I and the η_{max} are shown in Figure 11(d) and Table 3, respectively. As a combined consequence of lower P and lower Q_c, an even higher η_{max} is achieved for the segmented module. At T_h = 873 K, a very high η_{max} of ~11% is achieved at a current of 2.2 A. The testing of the segmented Bi_2Te_3/ns-PbTe module was performed three times to confirm its repeatability. All results of are in good agreement to each other, as shown in Figure S7 in the Supplementary Information

The simulated V_{oc}, R_{in}, P_{max}, Q_{oc} and η_{max} of segmented Bi_2Te_3/PbTe–MgTe (*p*-type)–Bi_2Te_3/PbTe (*n*-type) module are summarized in Table 3 along with the measured values. For ΔT of 590 K, the measured P_{max} and η_{max} are ~2.3 W and ~11%, which are ~10% and ~30% lower than the simulated values, P_{max} = 2.55 W and η_{max} = 15.6%, respectively. Like ns-PbTe module, the larger R_{in} and Q_{oc} values of the fabricated Bi_2Te_3/ns-PbTe module lead to lower values of measured P_{max} and η_{max}. The

measured R_{in} for ΔT of 590 K (~0.37 Ω) is ~5% larger than the ideal value of 0.35 Ω. The measured Q_{oc} for ΔT of 590 K (~16 W) is ~47% larger than the ideal value of 10.8 W. Again, the larger heat flow in the experiment is believed to stem from the parasitic radiation in the open space in the module. This implies that the experimentally determined conversion efficiency is underestimated even if we take the radiation heat losses from the side walls of thermoelectric legs into account. Further optimization of the interfaces between thermoelectric materials and electrodes and Bi_2Te_3 and ns-PbTe and geometrical configuration of module presumably will enable higher P and η.

Our work presented here paves a path for obtaining exceptionally high efficiency devices using newly developed nanostructured thermoelectric materials. Our future work aims at developing a multi-stage or functionally graded leg module which would cover a broader temperature range, providing higher average ZT and device efficiency.[81,82]

4. Conclusions

We successfully demonstrated that a comprehensive effort covering all aspects of thermoelectrics, *i.e.*, from materials to module, can realize high conversion efficiency in the new nanostructured PbTe-based systems. The dramatic enhancement in the ZT achieved in the nanostructured materials is mainly due to reduction in the lattice thermal conductivity through nanostructuring. The sintered compact of PbTe–2% MgTe doped with 4% Na used for *p*-type leg shows exceptionally high thermoelectric figure of merit ZT ~1.8 at 810 K and PbTe doped with 0.2% PbI_2 used for *n*-type legs shows high ZT ~1.4 at 750 K. We have successfully implemented these advanced thermoelectric materials in module development. The maximum conversion efficiency of

nanostructured PbTe (PbTe–MgTe (*p*-type)–PbTe (*n*-type)) module and segmented Bi_2Te_3/nanostructured PbTe (Bi_2Te_3/PbTe–MgTe (*p*-type)–Bi_2Te_3/PbTe (*n*-type)) module (each comprising eight *p*–*n* couples) reach very high values of 8.8% for temperature difference of 570 K and 11% for temperature difference of 590 K, respectively. These efficiencies are the highest ever reported for PbTe-based materials. The measured internal resistance and open-circuit heat flow of our modules is larger than the simulated values, leading to lower maximum conversion efficiency than expected. Therefore, as a next step we will focus on the further improvement of the electrical and thermal contacts between the nanostructured PbTe legs and Cu interconnecting electrodes in order to achieve >12% maximum conversion efficiency in the nanostructured PbTe-based module and > 15% maximum conversion efficiency in the segmented Bi_2Te_3/nanostructured PbTe module.

Author contributions

X.H. and P.J contributed equally to this work. M.O., A.Y. and M.G.K. designed the work. P.J., M.O., and M.K. conducted the synthesis and sintering of the materials and legs. P.J., M.O., and H.N. investigated the thermoelectric properties of the materials. K.N. and A.Y. fabricated and tested the module. X.H. and A.Y. conducted the power generation simulation of the module. M.O. P.J. X.H., A.Y, and M.G.K. analyzed the results and wrote the manuscript.

Conflict of interest

The authors have declared no conflicts of interest.

Acknowledgements

The authors express our thanks to Ms. Naoko Fujimoto of AIST for preparing the PbTe-based ingots and sintered compacts, Mr. Hiroyuki Takazawa of Thermal Management Materials and Technology Research Association (TherMAT) for testing the modules, and Mr. Noriyuki Saitou and Dr. Noriko Yoshizawa of National Institute of Advanced Industrial Science and Technology (AIST) for operating the transmission electron microscope. Material preparation and module fabrication were supported as part of the Japan-U.S. Cooperation Project for Research and Standardization of Clean Energy Technologies funded by the Ministry of Economy, Trade and Industry (METI). Module testing and three-dimensional finite-element simulation were supported as part of the International Cooperation Project for Research and Standardization of Clean Energy Technologies funded by METI. Priyanka Jood as an International Research Fellow of the Japan Society for the Promotion of Science acknowledges financial support from JSPS Grant Number 15F15068. At AIST, the work supported by the JSPS KAKENHI Grant Number 25420699. At Northwestern this was supported by the Department of Energy, Office of Science Basic Energy Sciences grant DE-SC0014520.

Corresponding author

Michihiro Ohta

ohta.michihiro@aist.go.jp (M.O.)

References

[1] Intergovernmental Panel on Climate Change, *Climate Change 2014: Synthesis Report, Fifth Assessment Report*, 2014.

[2] T. Kajikawa, in *Thermoelectrics Handbook: Macro to Nano*, ed. D.M. Rowe, CRC Press, Boca Raton, 2005, ch.50, pp.50-1–50-28.

[3] L.E. Bell, *Science*, 2008, **321**, 1457–1461.

[4] D. M. Rowe, in *Thermoelectrics and its Energy Harvesting: Modules, Systems, and Applications in Thermoelectrics*, ed. D. M. Rowe, CRC Press, Boca Raton, 2012, ch.23, pp.23-1–23-21.

[5] J. Yang, in *Thermoelectrics and its Energy Harvesting: Modules, Systems, and Applications in Thermoelectrics*, ed. D. M. Rowe, CRC Press, Boca Raton, 2012, ch.25, pp.25-1–25-15.

[6] H. J. Goldsmid, in *CRC Handbook of Thermoelectrics*, ed. D.M. Rowe, CRC Press, Boca Raton, 1995, ch.3, pp.19–25.

[7] J. P. Heremans, V. Jovovic, E. S. Toberer, A. Saramat, K. Kurosaki, A. Charoenphakdee, S. Yamanaka and G. J. Snyder, *Science*, 2008, **321**, 554–557.

[8] M. G. Kanatzidis, *Chem. Mater.*, 2010, **22**, 648–659.

[9] C. J. Vineis, A. Shakouri, A. Majumdar and M. G. Kanatzidis, *Adv. Mater.*, 2010, **22**, 3970.

[10] Y. Z Pei, X. Y. Shi, A. LaLonde, H. Wang, L. D. Chen and G. J. Snyder, *Nature*, 2011, **473**, 66–69.

[11] J. Q. He, M. G. Kanatzidis and V. P. Dravid, *Mater. Today*, 2013, **5**, 166–176.

[12] L. D. Zhao, V. P. Dravid and M. G. Kanatzidis, *Energy Environ. Sci.*, 2014, **7**, 251–268.

[13] B. C. Sales, D. Mandrus and R. K. Williams, *Science* 1996, **272**, 1325–1328.

[14] G. S. Nolas, D. T. Morelli and T. M. Tritt, *Annu. Rev. Mater. Sci.* 1999, **29**, 89–116.

[15] C. Uher, in *Thermoelectrics Handbook: Macro to Nano*, ed. D.M. Rowe, CRC Press, Boca Raton, 2005, ch.34, pp.34-1–34-17.

[16] X. Shi, J. Yang, J. R. Salvador, M. F. Chi, J. Y. Cho, H. Wang, S. Q. Bai, J. H. Yang, W. Q. Zhang and L. Chen, *J. Am. Chem. Soc.,* 2011, **133**, 7837–7846.

[17] G. S. Nolas, J. L. Cohn and G. A. Slack and S. B. Schujman, *Appl. Phys. Lett.*, 1998, **73**, 178–180.

[18] T. Takabatake, in *Thermoelectric Nanomaterials: Materials Design and Applications*, ed. K. Koumoto and T. Mori, Springer, Berlin, 2013, ch.2, pp.33–49.

[19] T. Takabatake, K. Suekuni, T. Nakayama and E. Kaneshita, *Rev. Mod. Phys.*, 2014, **86**, 669–716.

[20] S. Chen and Z.F. Ren, *Mater. Today*, 2010, **16**, 387–395.

[21] X. Yan, W. S. Liu, H. Wang, S. Chen, J. Shiomi, K. Esfarjani, H. Z. Wang, D. Wang, G. Chen and Z. F. Ren, *Energy Environ. Sci.*, 2012, **5**, 7543–7548.

[22] W. J. Xie, A. Weidenkaff, X. F. Tang, Q. G. Zhang, J. Poon and T. M. Tritt, *Nanomaterials*, 2012, **2**, 379–412.

[23] I. Terasaki, Y. Sasago and K. Uchinokura, *Phys. Rev. B*, 1997, **56**, R12685–R12687.

[24] R. Funahashi, I. Matsubara, H. Ikuta, T. Takeuchi, U. Mizutani and S. Sodeoka, *Jpn. J. Appl. Phys.*, 2000, **39**, L1127–L1129.

[25] K. Koumoto, I. Terasaki, T. Kajitani, M. Ohtaki and R. Funahashi, in *Thermoelectrics Handbook: Macro to Nano*, ed. D. M. Rowe, CRC Press, Boca Raton, 2005, ch.35, pp.35-1–35-15.

[26] K. Koumoto, Y. F. Wang, R. Z. Zhang, A. Kosuga and R. Funahashi, *Annu. Rev.*

Mater. Res., 2010, **40**, 363–394.

[27] K. Koumoto, R. Funahashi, E. Guilmeau, Y. Miyazaki, A. Weidenkaff, Y. F. Wang and C. L. Wan, *J. Am. Ceram. Soc.*, 2013, **96**, 1–23.

[28] S. Hébert, W. Kobayashi, H. Muguerra, Y. Bréard, N. Raghavendra, F. Gascoin, E. Guilmeau and A. Maignan, *Phys. Status Solidi A*, 2013, **210**, 69–81.

[29] K. Suekuni, K. Tsuruta, M. Kunii, H. Nishiate, E. Nishibori, S. Maki, M. Ohta, A. Yamamoto and M. Koyano, *J. Appl. Phys.*, 2013, **113**, 043712-1–043712-5.

[30] K. Suekuni, F. S. Kim, H. Nishiate, M. Ohta, H. I. Tanaka and T. Takabatake, *Appl. Phys. Lett.*, 2014, **105**, 132107-1–132107-4.

[31] Q. Tan, L.D. Zhao, J.F. Li, C.F. Wu, T.R. Wei, Z.B. Xing and M.G. Kanatzidis, *J. Mater. Chem. A.*, 2014, **2**, 17302–17306.

[32] P. Jood and M. Ohta, *Materials*, 2015, **8**, 1124–1149.

[33] C. L. Wan, X. K. Gu, F. Dang, T. Itoh, Y. F. Wang, H. Sasaki, M. Kondo, K. Koga, K. Yabuki, G. J. Snyder, R. G. Yang and K. Koumoto, *Nat. Mater.*, 2015, **14**, 622–627.

[34] A. D. LaLonde, Y. Z. Pei, H. Wang and G. J. Snyder, *Mater. Today*, 2011, **14**, 526–532.

[35] Yu. I. Ravich, B. A. Efimova and I. A. Smirnov, in *Semiconducting Lead Chalcogenides*, ed. L. S. Stil'bans, Plenum Press, New York, 1970, pp.13–41, 85–346.

[36] A. D. LaLonde, Y. Z. Pei and G. J. Snyder, *Energy Environ. Sci.*, 2011, **4**, 2090–2096.

[37] J. Androulakis, C. H. Lin, H. J. Kong, C. Uher, C. I. Wu, T. Hogan, B. A. Cook, T. Caillat, K. M. Paraskevopoulos and M. G. Kanatzidis, *J. Am. Chem. Soc*., 2007,

129, 9780–9788.

[38] J. Q. He, S. N. Girard, M. G. Kanatzidis and V. P. Dravid, *Adv. Funct. Mater.*, 2010, **20**, 764–772.

[39] K. Ahn, M. K. Han, J. Q. He, J. Androulakis, S. Ballikaya, C. Uher, V. P. Dravid and M. G. Kanatzidis, *J. Am. Chem. Soc*. 2010, **132**, 5227–5235.

[40] S. N. Girard, J. Q. He, C. P. Li, S. Moses, G. Y. Wang, C. Uher, V. P. Dravid and M. G. Kanatzidis, *Nano Lett.*, 2010, **10**, 2825–2831.

[41] K. Biswas, J. Q. He, Q. C. Zhang, G. Y. Wang, C. Uher, V. P. Dravid and M. G. Kanatzidis, *Nat. Chem*., 2011, **3**, 160–166.

[42] K. Biswas, J. Q. He, G. Wang, S. -H. Lo, C. Uher, V. P. Dravid and M. G. Kanatzidis, *Energy Environ. Sci*., 2011, **4**, 4675.

[43] J. Q. He, J. Androulakis, M. G. Kanatzidis, and V. P. Dravid, *Nano Lett*, 2012, **12**, 343–347.

[44] M. Ohta, K. Biswas, S. H. Lo, J. Q. He, D. Y. Chung, V. P. Dravid and M. G. Kanatzidis, *Adv. Energy Mater.*, 2012, **2**, 1117–1123.

[45] K. Ahn, K. Biswas, J. Q. He, I. Chung, V. Dravid and M.G. Kanatzidis, *Energy Environ. Sci*., 2013, **6**, 1529–1537.

[46] H. J. Wu, L. D. Zhao, F. S. Zheng, D. Wu, Y. L. Pei, X. Tong, M. G. Kanatzidis and J. Q. He, *Nat. Commun.*, 2014, **5**, 4515-1–4515-9.

[47] K. Biswas, J. Q. He, I. D. Blum, C. I. Wu, T. P. Hogan, D. N. Seidman, V. P. Dravid and M. G. Kanatzidis, *Nature*, 2012, **489**, 414–418.

[48] L. D. Zhao, H. J. Wu, S. Q. Hao, C. I. Wu, X. Y. Zhou, K. Biswas, J. Q. He, T. P. Hogan, C. Uher, C. Wolverton, V. P. Dravid and M. G. Kanatzidis, *Energy Environ. Sci.*, 2013, **6**, 3346–3355.

[49] K. F. Hsu, S. Loo, F. Guo, W. Chen, J. S. Dyck, C. Uher, T. Hogan, E. K. Polychroniadis and M. G. Kanatzidis, *Science*, 2004, **303**, 818-821.

[50] T. P. Hogan, A. Downey, J. Short, J. D'Angelo, C.-I. Wu, E. Quarez, J. Androulakis, P. F. P. Poudeu, J. R. Sootsman, D. Y . Chung, M. G. Kanatzidis, S. D. Mahanti, E. J. Timm, H. Schock, F. Ren, J. Johnson and E. D. Case, *J. Electron. Mater.*, 2007, **36**, 704–710.

[51] J. D'angelo, E. D. Case, N. Matchanov, C. Wu, T. P. Hogan, J. Barnard, C. Cauchy, T. Hendricks and M. G. Kanatzidis, *J. Electron. Mater.*, 2011, **40**, 2051–2062.

[52] G. L. Bennett, in *CRC Handbook of Thermoelectrics*, ed. D.M. Rowe, CRC Press, Boca Raton, 1995, ch.41, pp.515–537.

[53] T. Caillat, J.-P. Fleurial, G. J. Snyder and A. Borshchevsky, in *Proceedings of 20th International Conference on Thermoelectrics*, IEEE, Piscataway, 2001, pp.282–285.

[54] H. Kaibe, I. Aoyama, M. Mukoujima, T. Kanda, S. Fujimoto, T. Kurosawa, H. Ishimabushi, K. Ishida, L. Rauscher, Y. Hata and S. Sano, in *Proceedings of 24th International Conference on Thermoelectrics*, IEEE, Piscataway, 2005, pp. 227–232.

[55] Y. Hori and T. Ito, in *Proceedings of 25th International Conference on Thermoelectrics,* IEEE, Piscataway, 2006, pp. 642–645.

[56] J. Q. Guo, H. Y. Geng, T. Ochi, S. Suzuki, M. Kikuchi, Y. Yamaguchi and S. Ito, *J. Electron. Mater.*, 2012, **41**, 1036–1042.

[57] A. J. Muto, J. Yang, B. Poudel, Z. F. Ren and G. Chen, *Adv. Energy Mater.*, 2013, **3**, 245–251.

[58] J. R. Salvador, J. Y. Cho, Z. Ye, J. E. Moczygemba, A. J. Thompson, J. W. Sharp, J.

D. Koenig, R. Maloney, T. Thompson, J. Sakamoto, H. Wang and A. A. Wereszczak, *Phys. Chem. Chem. Phys.*, 2014, **16**, 12510–12520.

[59] T. Takabatake, in *Thermoelectric Nanomaterials: Materials Design and Application*, ed. K. Koumoto and T. Mori, Springer, Heidelberg, 2013, ch.2, pp.33–49.

[60] D. Kraemer, J. Sui, K. McEnaney, H. Zhao, Q. Jie, Z. F. Ren and G. Chen, *Energy Environ. Sci.*, 2015, **8**, 1299–1308.

[61] N. B. Elsner, *MRS Proceedings*, 1991, **234**, 167–178.

[62] A. Singh, S. Bhattacharya1, C. Thinaharan, D. K. Aswal, S. K. Gupta, J. V. Yakhmi and K. Bhanumurthy, *J. Phys. D: Appl. Phys.*. 2009, **42**, 015502-1–015502-6.

[63] H. Y. Xia, F. Drymiotis, C. L. Chen, A. P. Wu and G. J. Snyder, *J. Mater. Sci.*, 2014, **49**, 1716–1723.

[64] H. Y. Xia, C. L. Chen, F. Drymiotis, A. P. Wu, Y. Y. Chen and G. J. Snyder, *J. Electron. Mater.*, 2014, **43**, 4064–4069.

[65] H. Wang, R. McCarty, J. R. Salvador, A. Yamamoto and J. König, *J. Electron. Mater.*, 2014, **43**, 2274–2286.

[66] D. Ebling, M. Jaegle, M. Bartel, A. Jacquot and H. Böttner, *J. Electron. Mater.*, 2009, **38**, 1456–1461.

[67] E. Sandoz-Rosado and R. J. Stevens, *J. Electron. Mater.*, 2010, **39**, 1848–1855.

[68] W. Wijesekara, L. Rosendahl, D. R. Brown and G. Snyder, *J. Electron. Mater.*, 2015, **44**, 1834–1845.

[69] X. K. Hu, A. Yamamoto, M. Ohta, and H. Nishiate, *Rev. Sci. Instrum.*, 2015, **86**, 045103:1–7.

[70] X. K. Hu, H. Takazawa, K. Nagase, M. Ohta and A. Yamamoto, *J. Electron. Mater.*,

2015, **44**, 3637–3645.

[71] B. Sherman, R. R. Heikes and R. W. Ure, *J. Appl. Phys*., 1960, **31**, 1–16.

[72] J. Q. He, J. R. Sootsman, S. N. Girard, J.-C. Zheng, J. Wen, Y. Zhu, M. G. Kanatzidis and V. P. Dravid, *J. Am. Chem. Soc*., 2010, **132**, 8669–8675.

[73] H. Z. Wang, Q. Y. Zhang, B. Yu, W. S. Liu, G. Chen and Z. F. Ren, *J. Mater. Res.,* 2011, **26**, 912–916.

[74] P. Jood, M. Ohta, M. Kunii, X. Hu, H. Nishiate, A. Yamamoto and M. G. Kanatzidis, *J. Mater. Chem. C*. DOI: 10.1039/C5TC01652E.

[75] K. Ahn, C. Li, C. Uher and M. G. Kanatzidis, *Chem. Mater.*, 2009, **21**, 1361–1367.

[76] J. R. Sootsman, H. Kong, C. Uher, J. D'Angelo, C.-I. Wu, T. P. Hogan, T. Caillat and M. G. Kanatzidis, *Angew. Chem. Int. Ed.*, 2008, **47**, 8618–8622.

[77] A. F. May, J.-P. Fleurial and G. J. Snyder, *Phys. Rev. B*, 2008, **78**, 125205.

[78] S. Johnsen, J. He, J. Androulakis. V. P. Dravid, I. Todorov, D. Y. Chung and M. G. Kanatzidis, *J. Am. Chem. Soc*., 2011, **133**, 3460–3470.

[79] E. Sandoz-Rosado and R. J. Stevens, *J. Electron. Mater.*, 2009, **38**, 1239–1244.

[80] R.B. Bird, W.E. Stewart and E.N. Lightfoot, in *Transport Phenomena*, John Wiley & Sons, New York, 1960, pp.426–455.

[81] B. A. Cook, T. E. Chan, G. Dezsi, P. Thomas, C. C. Koch, J. Poon, T. Tritt and R. Venkatasubramanian, J. Electron. Mater., 2015, 44, 1936–1942.

[82] E. Hazan, O. Ben-Yehuda, N. Madar and Y. Gelbstein, Adv. Energy. Mater., 2015, 5, 1500272:1–8.

Figure Captions

Figure 1. Maximum conversion efficiency (η_{max}) as function of the temperature difference (ΔT) over mid-temperature range for the nanostructured PbTe (ns-PbTe)-based module and segmented Bi_2Te_3/nanostructured PbTe (Bi_2Te_3/ns-PbTe) module developed in this study and important milestones achieved in previous studies, including segmented Bi_2Te_3/Ag–Pb–Sn–Sb–Te (LASTT) (*p*-type) and Bi_2Te_3/Ag–Pb–Sb–Te (LAST) (*n*-type),[51] PbTe,[52] segmented Bi_2Te_3/skutterudite,[53] Bi_2Te_3,[54] cascaded Bi_2Te_3/Mn–Si (*p*-type) and Bi_2Te_3/Mg_2Si (*n*-type),[54] cascaded Bi_2Te_3/PbTe[55] skutterudite[56–58], segmented Bi_2Te_3/clathrate[59], and MgAgSb[60].

Figure 2. Fabrication of nanostructured PbTe (PbTe–MgTe (*p*-type)–PbTe (*n*-type)) module and segmented segmented Bi_2Te_3/nanostructured PbTe (Bi_2Te_3/PbTe–MgTe (*p*-type)–Bi_2Te_3/PbTe (*n*-type)) module . The modules were prepared by: (a) polishing, then (b) and (c) cutting, and finally (d)–(g) assembling the components.

Figure 3. Module testing system used for electrical power output and conversion efficiency measurements of thermoelectric modules.

Figure 4. Powder X-ray diffraction patterns for PbTe–2% MgTe doped with 4% Na (*p*-type) and PbTe doped with 0.2% PbI_2 (*n*-type).

Figure 5. Transmission electron microscopy (TEM) bright field images and electron diffraction patterns along [001] zone axis for (a) *p*-type PbTe–2% MgTe doped with 4%

Na and (b) *n*-type PbTe doped with 0.2% PbI_2. (c) High-magnification TEM image of *p*-type PbTe showing spherical nanoprecipitates (indicated by arrows) in [111] and showing disk-like nanostructures (dotted circle) in [001]. (d) High-magnification TEM image of *n*-type PbTe showing disk-like nanostructures in [001]. (e) High-angle annular dark-field scanning transmission electron microscope image of *p*-type PbTe showing MgTe microcrystals (f) Energy dispersive X-ray spectroscopy of the microcrystals shown in (e).

Figure 6. Temperature dependence of the (a) Seebeck coefficient (S), (b) electrical resistivity (ρ), (c) power factor (S^2/ρ), and (d) total thermal conductivity (κ_{total}) and lattice thermal conductivity (κ_{lat}) for the *p*-type PbTe–2% MgTe doped with 4% Na and *n*-type PbTe doped with 0.2% PbI_2.

Figure 7. Temperature dependence of the thermoelectric figure of merit (ZT) for *p*-type PbTe–2% MgTe doped with 4% Na and *n*-type PbTe doped with 0.2% PbI_2.

Figure 8. Measured terminal voltage (V), electrical power output (P), heat dissipation from module at the cold side (Q_c), and conversion efficiency (η) of the nanostructured PbTe–MgTe (*p*-type)–PbTe (*n*-type) module as functions of electrical current (I). While the hot-side temperature (T_h) was changed from 873 K to 573 K, the cold-side temperature (T_c) was maintained at 303 K.

Figure 9. Typical results of numerical simulations for the nanostructured PbTe-based module (PbTe–2% MgTe doped with 4% Na (*p*-type) and PbTe doped with 0.2% PbI_2

(*n*-type)) for hot side at 873 K and cold side at 303 K and load conductivity of 4.5×10^2 S/cm. (a) Geometrical configuration, (b) temperature (T), (c) electrical potential (V), (d) z-component of the heat flux (q), (e) Joule heat (J^2/σ), and (d) thermoelectric figure of merit (ZT). Dimensions of the module are in mm.

Figure 10. Simulated terminal voltage (V), electrical power output (P), heat dissipation from module at the cold side (Q_c), and conversion efficiency (η) of the nanostructured PbTe–MgTe (*p*-type)–PbTe (*n*-type) module as functions of electrical current (I). While the hot-side temperature (T_h) was changed from 873 K to 573 K, the cold-side temperature (T_c) was maintained at 303 K.

Figure 11. Measured terminal voltage (V), electrical power output (P), heat dissipation from module at the cold side (Q_c), and conversion efficiency (η) of the segmented Bi_2Te_3/nanostructured PbTe (Bi_2Te_3/PbTe–MgTe (*p*-type)–Bi_2Te_3/PbTe (*n*-type)) module as functions of electrical current (I). While the hot-side temperature (T_h) was changed from 873 K to 573 K, the cold-side temperature (T_c) was maintained at 283 K.

Table 1. Room-temperature carrier concentration (n), hall coefficient (R_H) and electron mobility (μ) obtained from the PbTe–2% MgTe doped with 4% Na and PbTe doped with 0.2% PbI_2.

Sample	n (10^{19} cm^{-3})	R_H (10^{-7} m^3 C^{-1})	μ (cm^2 V^{-1} s^{-1})
PbTe–2% MgTe doped with 4% Na	9.5	0.65	130
PbTe doped with 0.2% PbI_2.	3.9	−1.6	320

Table 2 Measured and simulated open-circuit voltage (V_{OC}), internal resistance (R_{in}), maximum power output (P_{max}), open-circuit heat flow (Q_{oc}), maximum conversion efficiency (η_{max}) of the nanostructured PbTe–MgTe (*p*-type)–PbTe (*n*-type) module. While the hot-side temperature (T_h) was varied from 873 K to 573 K, the cold-side temperature (T_c) was maintained at 303 K.

		Measured values					Simulated values				
T_h (K)	T_c (K)	V_{oc} (V)	R_{in} (Ω)	P_{max} (W)	Q_{oc} (W)	η_{max} (%)	V_{oc} (V)	R_{in} (Ω)	P_{max} (W)	Q_{oc} (W)	η_{max} (%)
873	303	1.47	0.152	3.55	30.9	8.8	1.59	0.137	4.71	27.3	12.2
773	303	1.14	0.130	2.47	27.4	7.2	1.20	0.112	3.26	24.1	10.0
673	303	0.86	0.115	1.60	23.8	5.6	0.85	0.091	1.96	20.7	7.4
573	303	0.57	0.096	0.84	19.69	3.7	0.53	0.074	0.96	17.0	4.7

Table 3 Measured and simulated open-circuit voltage (V_{OC}), internal resistance (R_{in}), maximum power output (P_{max}), open-circuit heat flow (Q_{oc}), maximum conversion efficiency (η_{max}) of the segmented Bi_2Te_3/PbTe–MgTe (*p*-type)–Bi_2Te_3/PbTe (*n*-type) module. While the hot-side temperature (T_h) was varied from 873 K to 573 K, the cold-side temperature (T_c) was maintained at 283 K.

		Measured values					Simulated values				
T_h (K)	T_c (K)	V_{oc} (V)	R_{in} (Ω)	P_{max} (W)	Q_{oc} (W)	η_{max} (%)	V_{oc} (V)	R_{in} (Ω)	P_{max} (W)	Q_{oc} (W)	η_{max} (%)
873	283	1.86	0.371	2.34	15.8	11	1.89	0.35	2.55	10.8	15.6
773	283	1.53	0.327	1.82	13.4	10	1.53	0.311	1.90	9.1	13.9
673	283	1.21	0.286	1.29	11.0	8.9	1.17	0.274	1.28	7.6	11.8
573	283	0.88	0.246	0.79	8.3	7.3	0.83	0.24	0.76	6.0	9.1

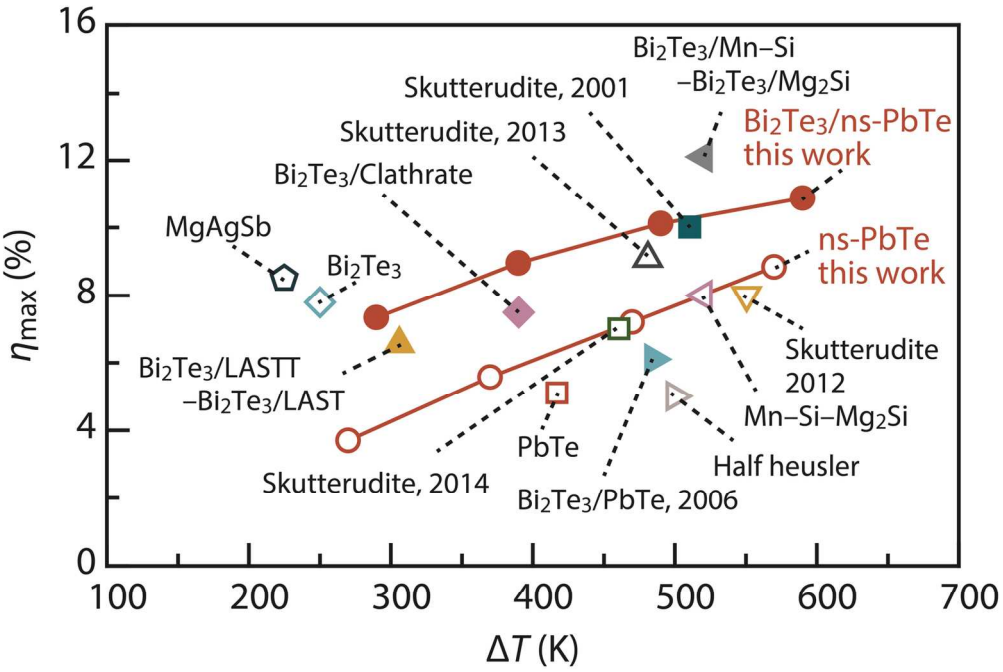

Fig.1

149x117mm (300 x 300 DPI)

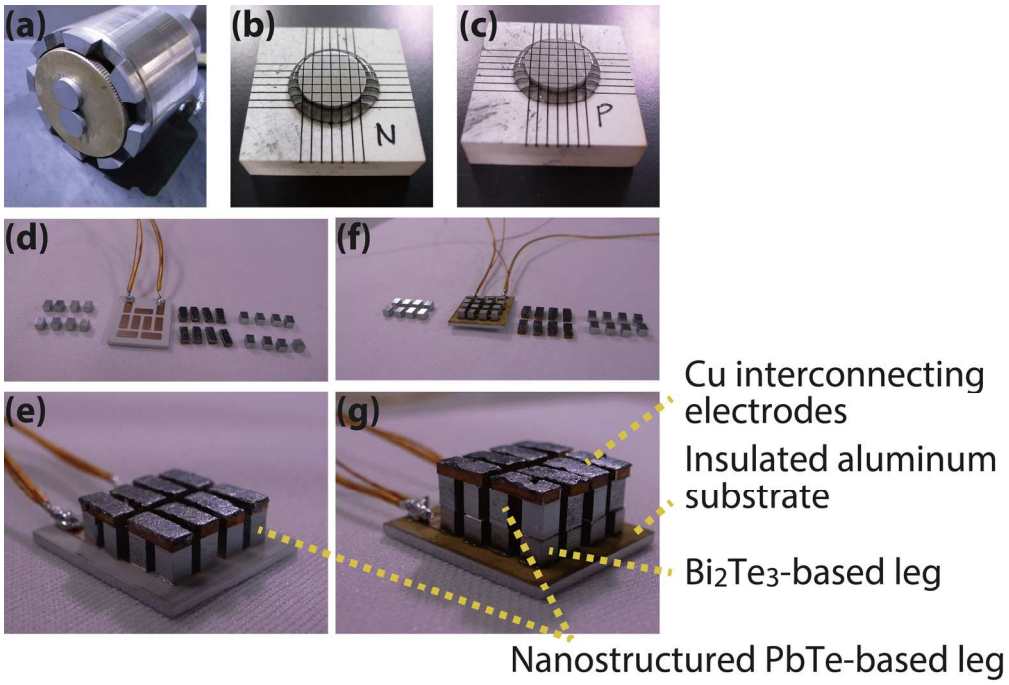

Fig.2

172x149mm (300 x 300 DPI)

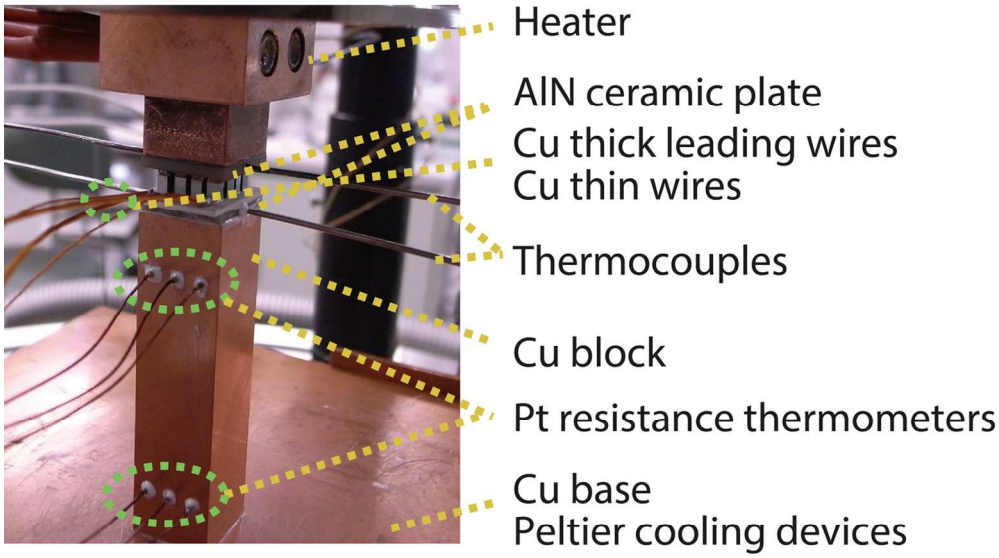

Fig.3

129x94mm (300 x 300 DPI)

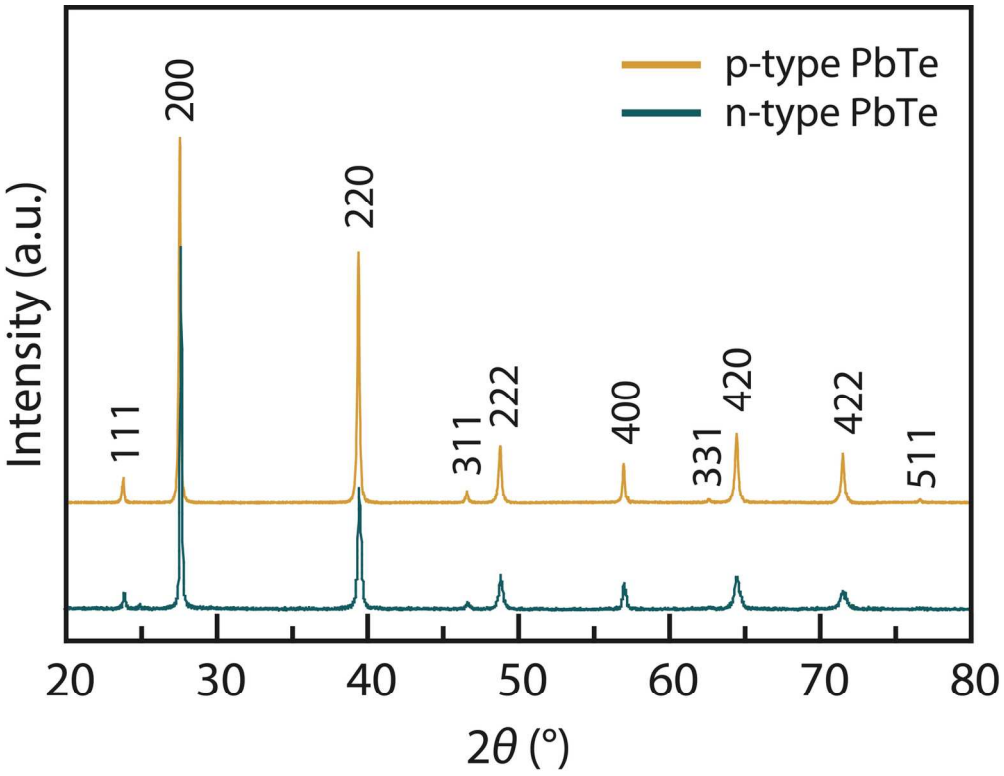

Fig.4

146x143mm (300 x 300 DPI)

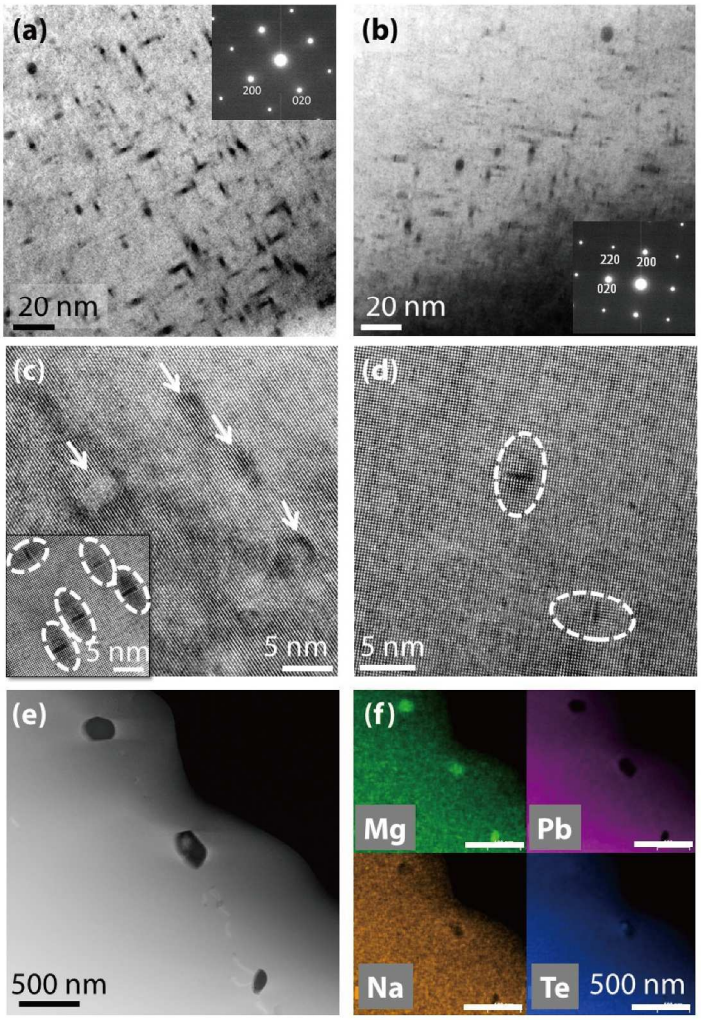

Fig.5

306x519mm (300 x 300 DPI)

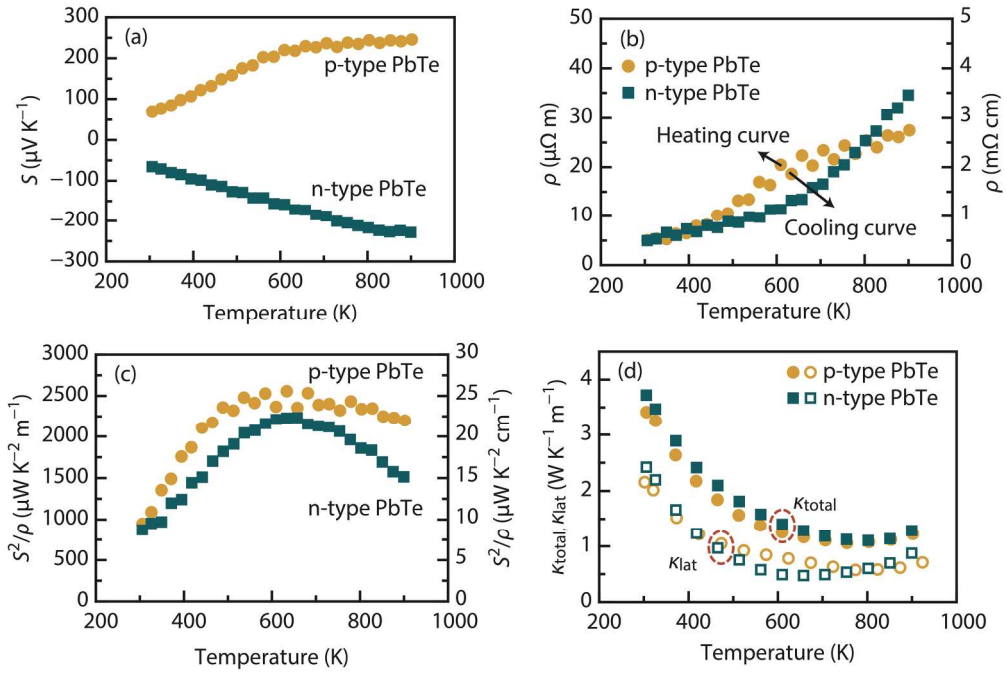

Fig.6

204x150mm (300 x 300 DPI)

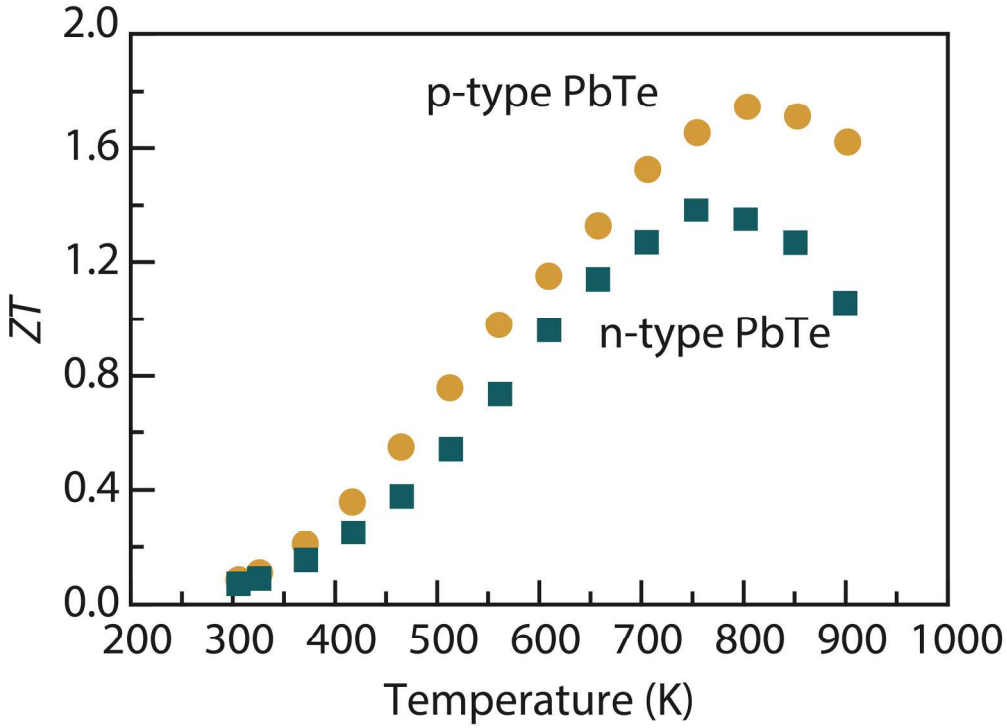

Fig.7

195x208mm (300 x 300 DPI)

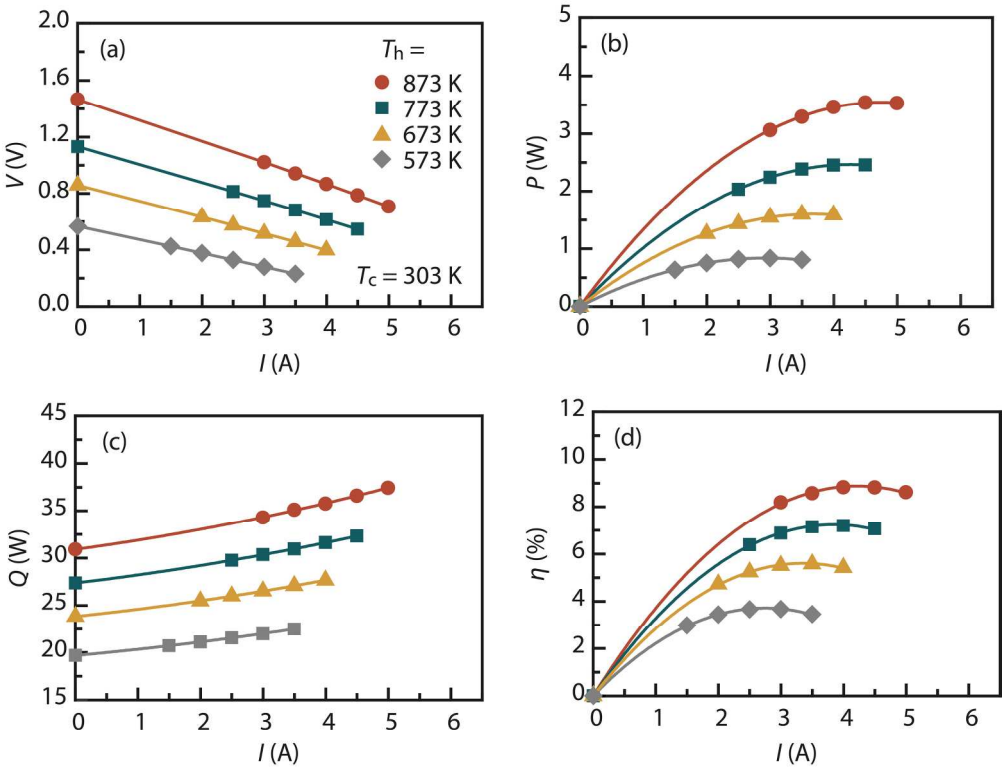

Fig.8

206x171mm (300 x 300 DPI)

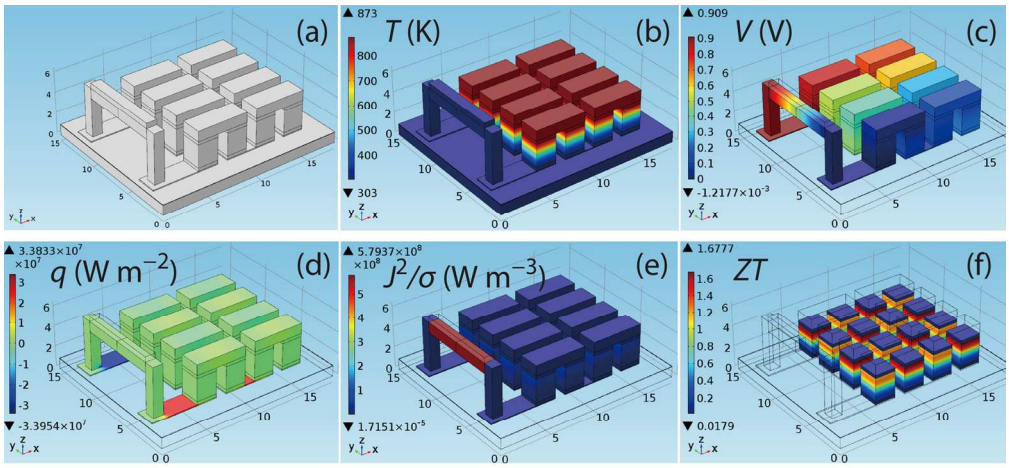

Fig.9

144x104mm (300 x 300 DPI)

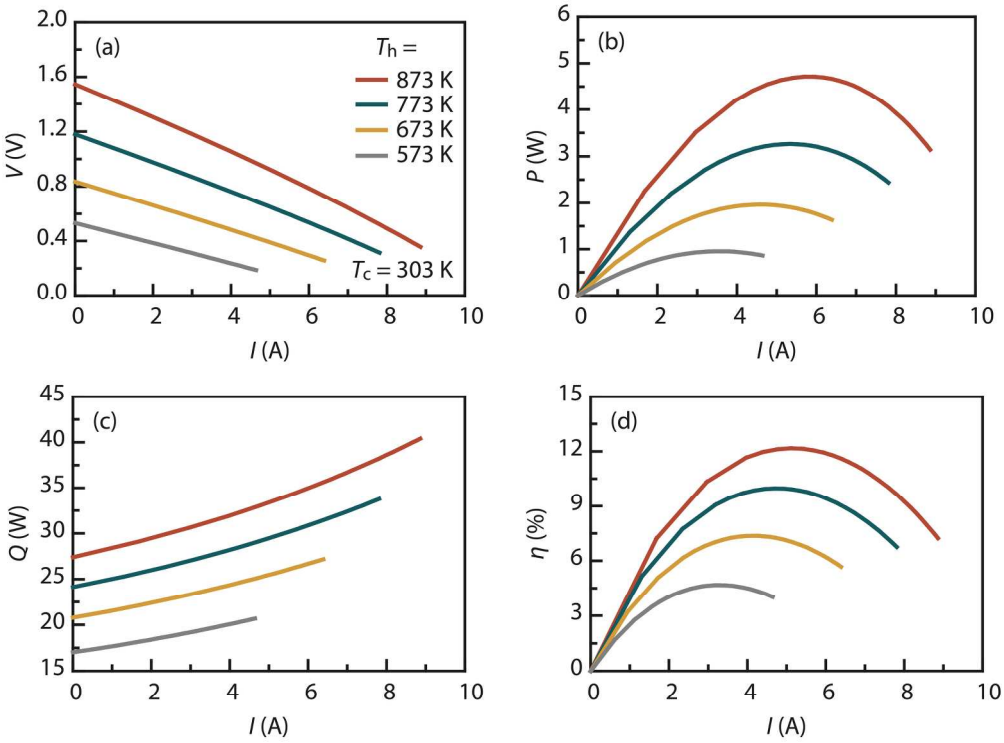

Fig.10

203x161mm (300 x 300 DPI)

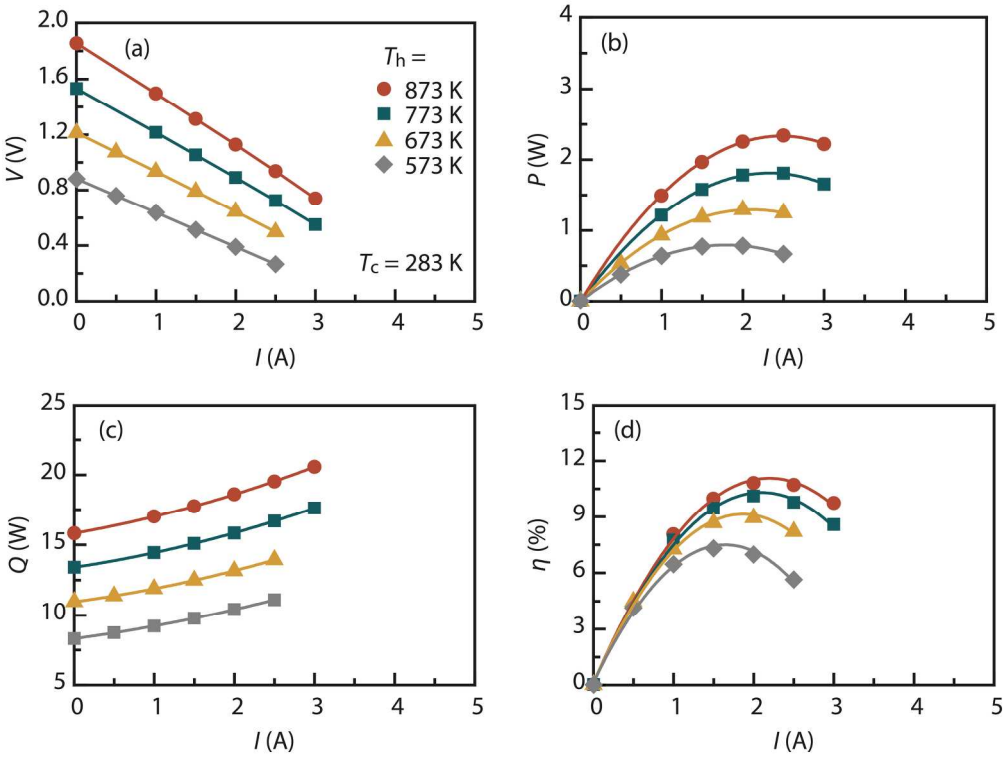

Fig.11

205x168mm (300 x 300 DPI)